catalysts

MDPI

Article

Effects of Lanthanide Doping on the Catalytic Activity and Hydrothermal Stability of Cu-SAPO-18 for the Catalytic Removal of NO_x (NH_3-SCR) from Diesel Engines

Qi Gao [1], Shuai Han [1], Qing Ye [1,*], Shuiyuan Cheng [1], Tianfang Kang [1] and Hongxing Dai [2,*]

[1] Key Laboratory of Beijing on Regional Air Pollution Control, Department of Environmental Science, College of Environmental and Energy Engineering, Beijing University of Technology, Beijing 100124, China; gaoq950103@gmail.com (Q.G.); hanshuai@emails.bjut.edu.cn (S.H.); chengsy@bjut.edu.cn (S.C.); kangtf@bjut.edu.cn (T.K.)

[2] Beijing Key Laboratory for Green Catalysis and Separation, Key Laboratory of Beijing on Regional Air Pollution Control, and Laboratory of Catalysis Chemistry and Nanoscience, Department of Chemistry and Chemical Engineering, College of Environmental and Energy Engineering, Beijing University of Technology, Beijing 100124, China

* Correspondence: yeqing@bjut.edu.cn (Q. Y); hxdai@bjut.edu.cn (H.D.); Tel.: +86-10-6739-1659 (Q.Y.); +86-10-6739-6118 (H.D.); Fax: +86-10-6739-1983 (Q.Y.); +86-10-6739-1983 (H.D.)

Received: 15 January 2020; Accepted: 15 March 2020; Published: 17 March 2020

Abstract: Lanthanide (La, Ce, Nd, Gd, Tb, Ho or Lu)-doped Cu-SAPO-18 samples were prepared using the ion-exchange method. Physicochemical properties of the samples were systematically characterized by a number of analytical techniques, and the effects of lanthanide doping on catalytic activity and hydrothermal stability of the Cu-SAPO-18 catalysts for the NH_3-SCR reaction were examined. It is shown that the doping of lanthanide elements could affect the interaction between the active components (copper ions) and the AEI-structured SAPO-18 support. The inclusion of some lanthanides significantly slowed down hydrolysis of the catalyst during hydrothermal aging treatment process, leading to an enhanced catalytic activity at both low and high temperatures and hydrothermal stability. In particular, Ce doping promoted the Cu^{2+} ions to migrate to the energetically favorable sites for enhancement in catalytic activity, whereas the other lanthanide ions exerted little or an opposite effect on the migration of Cu^{2+} ions. Additionally, Ce doping could improve hydrothermal stability of the Cu-SAPO-18 catalyst by weakening hydrolysis of the catalyst during the hydrothermal aging treatment process. Ce doping increased the catalytic activity of Cu-SAPO-18 at low and high temperatures, which was attributed to modifications of the redox and/or isolated Cu^{2+} active centers.

Keywords: SAPO-18-incorporated Cu catalyst; lanthanide doping; selective catalytic reduction; NH_3-SCR; hydrothermal stability

1. Introduction

Nitrogen oxides (NO_x) are one of the main pollutants to the atmosphere. NO_x is emitted from fossil fuels burning, nitric acid and plating industries, and automotive vehicles [1,2], in which NO_x emission from vehicle exhaust has become a major source of air pollutants [3]. Selective catalytic reduction of NH_3 (NH_3-SCR) over different catalysts has been extensively studied. The SCR of NO_x with ammonia is one of the most widely applied emission control technologies [4,5]. The key issue of such a NH_3-SCR technology is the availability of high-performance catalysts [6]. In recent decades, the V_2O_5−WO_3/TiO_2 catalysts show high catalytic activities and SO_2 poisoning resistance, and are

widely used in the NH_3-SCR reaction [7]. These catalyst systems, however, have some disadvantages, for example, generation of NO_x due to oxidation of ammonia at high temperatures, narrow activity window, and low hydrothermal resistance [8,9]. Therefore, it is urgent to develop catalysts with good hydrothermal resistance, wide active windows, and high nitrogen selectivity.

In the past two decades, the zeolites with large and medium pore sizes (such as zeolite Y, zeolite beta and ZSM-5) have received much attention [10,11]. The most extensive research has focused on the copper ion-exchanged ZSM-5, which showed good catalytic activity for direct NO decomposition and NH_3-SCR reaction [12]. However, a big problem of this catalyst is its poor hydrothermal stability [8]. Nowadays, copper-based zeolites with small pore structures (such as Cu-SSZ-13 and Cu-SAPO-34), especially the CHA structures, have attracted much attention in eliminating NO_x pollution since they possess good hydrothermal aging stability and NH_3-SCR performance [13,14]. The AEI-structure is similar to the CHA-structure. Previously, our team found that Cu-SAPO-18 possessed excellent performance for the SCR of NO_x, excellent hydrothermal aging stability and poisoning hydrocarbons resistance [15]. The SAPO-18-supported Cu catalysts, however, have drawbacks of hydrothermal deterioration, narrow activity windows, and nonselective NH_3 oxidation which produces NO_x and hence restricts further commercial applications [16]. Since lanthanide oxides possess excellent oxygen storage capacity and unique redox properties [17], lanthanide-doped catalysts have been widely investigated for various reactions. Samojeden et al. found that the sample of Fe-modified vermiculite doped with Ho showed better activity as compared with the Cu-modified vermiculite sample [18].

In this work, lanthanide (La, Ce, Nd, Gd, Tb, Ho or Lu)-doped Cu-SAPO-18 samples were prepared by the ion-exchange method. Effects of lanthanide doping on NH_3-SCR activity and hydrothermal stability of Cu-SAPO-18 were investigated. The XRD, BET, ^{27}Al NMR, NH_3-TPD, and in situ DRIFTS-NH_3 adsorption were used to determine the changes in textural properties and acid density of Cu-SAPO-18 possibly induced by the doping of lanthanides. In addition, the interaction between copper and lanthanide was clarified by the XPS characterization, and reduction behaviour of the copper species in the catalyst was measured by the H_2-TPR technique.

2. Results

2.1. NH_3-SCR Performance and Hydrothermal Stability

In order to eliminate the influence of calcination temperature, catalytic activities of the Cu-SAPO-18 and Ce-Cu-SAPO18 samples calcined at 500 and 600 °C were measured, as shown in Figure S1. NO conversion over Cu-SAPO-18 increased in the temperature range of 100–300 °C, the maximum conversion (91.5%) was reached at 300 °C, and dropped subsequently, whereas NO conversion decreased to 66.4% at 600 °C, as shown in Figure 1a. The decrease in NO conversion might be caused by the reaction of partial amount of NH_3 with O_2 to form NO_x, which reduced the conversion of nitrogen oxides. NH_3-SCR performance over the fresh M-Cu-SAPO-18 sample is also shown in Figure 1a. As expected, the simultaneously M- and Cu-exchanged catalysts exhibited different activities, as compared with the Cu-exchanged catalyst. It is interesting to note that the Ce-Cu-SAPO-18 and Tb-Cu-SAPO-18 catalysts showed higher activities than the Cu-SAPO-18 catalyst in the whole temperature range, which might be due to the synergistic effect. NO conversion was over 90 % in the range of 200−550 °C, and NO conversion at 600 °C reached to 89.9% over Ce-Cu-SAPO-18 and 86.7% over Tb-CuSAPO-18. After the doping of Lu or Ho, the activity increased only at high temperatures, and NO conversion at 600 °C was ca. 80.2% over Lu-Cu-SAPO-18 and 82.7% over Ho-Cu-SAPO-18. As can be seen from Figure 1a, compared with Cu-SAPO-18, the activity over Gd-Cu-SAPO-18 and La-Cu-SAPO-18 decreased at low temperatures (e.g., only 78.7 and 70.1% at 200 °C, respectively). Therefore, the introduction of Ce or Tb increased the catalytic activity in the whole temperature range and the high activity was maintained even up to 600 °C.

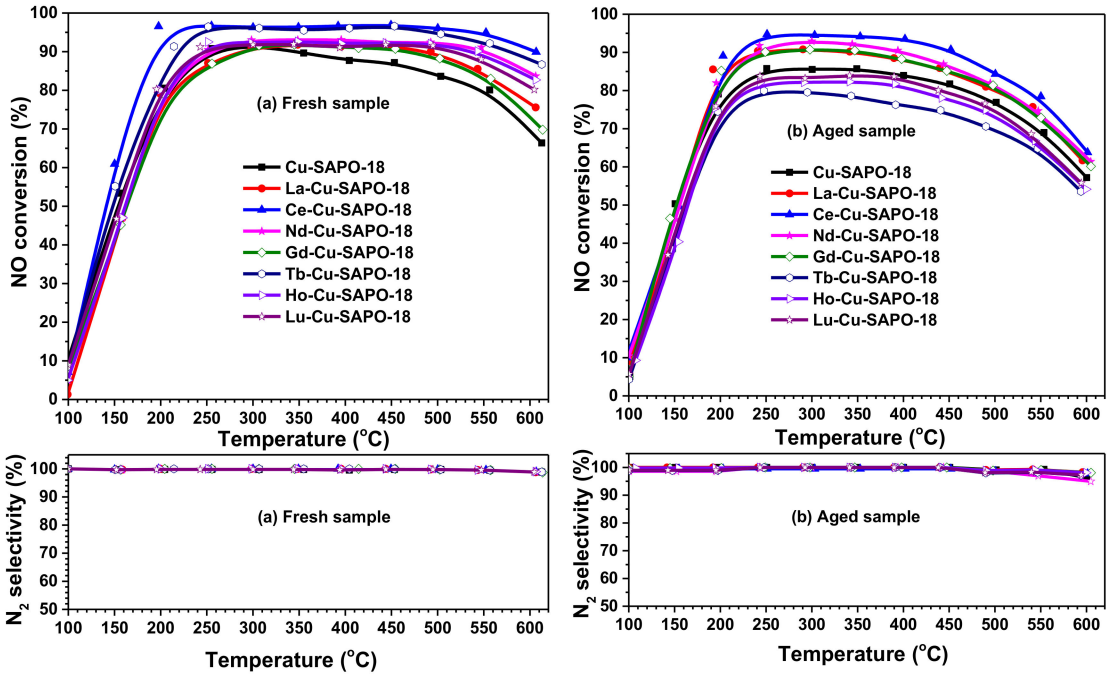

Figure 1. NO conversion and N_2 selectivity as a function of temperature for the selective catalytic reduction of NH_3 (NH_3-SCR) reaction over the (**a**) fresh and (**b**) hydrothermally aged Cu-SAPO-18 and M-Cu-SAPO-18 samples at a gas hour space velocity (GHSV) of 130,000 h^{-1}. The reactant feed composition: 500 ppm NO, 500 ppm NH_3, 14 vol % O_2, 5 vol % H_2O, and N_2 (balance).

In order to probe the hydrothermal stability, the above mentioned eight catalysts were further treated in air with 10 vol% H_2O at 850 °C for 12 h. The NH_3-SCR activities over the aged catalysts are shown in Figure 1b. For the Cu-SAPO-18-aged sample, NO conversion decreased significantly (85.7 % at 350 °C), especially at higher temperatures (400−600 °C). After doping lanthanide elements, however, NO conversions over the samples changed differently before and after hydrothermal aging treatment. Over the Tb-Cu-SAPO-18-aged, Ho-Cu-SAPO-18-aged, and Lu-Cu-SAPO-18-aged samples, NO conversions decreased obviously (e.g., 78.6, 82.3, and 83.9% at 350 °C, respectively), which were lower than those over the corresponding fresh samples and the Cu-SAPO-18-aged sample in the whole temperature range. The results indicate that the addition of Tb, Ho or Lu to Cu-SAPO-18 resulted in a worse performance after hydrothermal aging treatment. Over the La-Cu-SAPO-18-aged, Nd- Cu-SAP-18-aged, and Gd-Cu-SAPO-18-aged samples, NO conversions decreased slightly (e.g., 90.2, 92.2, and 90.5% at 350 °C, respectively), which were lower than those over the corresponding fresh samples but higher than that the fresh Cu-SAPO-18 sample, especially at low temperatures (200−350 °C). The results suggest that the doping of La, Nd or Gd improved the hydrothermal aging ability of Cu-SAPO-18. In particular, even after hydrothermal aging treatment of the Ce-Cu-SAPO-18, its catalytic activity was still high (NO conversion was over 90% at 250−400 °C). At higher temperatures, NO conversion decreased slightly, but still retained 80−90% at 400−550 °C. It is concluded that the hydrothermal stability of Ce-Cu -SAPO-18 was the highest among all of the lanthanide-doped Cu-SAPO-18 samples.

Figure 2a shows the Arrhenius plots for the NH_3-SCR reaction in the low-temperature range over the fresh Cu-SAPO-18 and M-Cu-SAPO-18 catalysts. Figure 3 shows the apparent activation energies obtained over all of the samples. The change in activation energy of M-Cu-SAPO-18 was similar to that of Cu-SAPO-18, indicating that the nature of the Cu ions and SCR reaction mechanism were not altered after the doping of lanthanides. As shown in Figure 3, the activation energy decreased in the order of Lu-Cu-SAPO-18 > Ho-Cu- SAPO-18 > Cu-SAPO-18 > La-Cu-SAPO-18 > Nd-Cu-SAPO-18 > Gd-Cu-SAPO-18 > Tb-Cu-SAPO-18 > Ce-Cu-SAPO-18. Specifically, after the introduction of Ce or Tb,

the activation energy decreased (as compared with Cu-SAPO-18), which indicates that Ce or Tb doping improved the catalytic activity, in good agreement with the NH_3-SCR performance. Figure 2b shows the Arrhenius plots for the NH_3-SCR reaction in the low-temperature range over the hydrothermally aged CuSAPO-18 and M-CuSAPO-18 catalysts. After hydrothermal aging treatment, the activation energy declined in the sequence of Tb-Cu-SAPO-18-aged > Cu-SAPO-18-aged > Gd-Cu- SAPO-18-aged > La-Cu-SAPO-18-aged > Lu-Cu-SAPO-18-aged > Ho-Cu-SAPO- 18-aged > Nd-Cu-SAPO-18-aged > Ce-Cu-SAPO-18-aged. Compared with the corresponding fresh sample, the Ce-Cu-SAPO-18-aged sample showed a slight change in catalytic activity, but the other aged samples exhibited an obvious decrease in catalytic activity. The activation energy of Ce-Cu-SAPO-18 after hydrothermal aging treatment increased slightly from 28.5 to 31.1 kJ/mol. The hydrothermally aged Tb-Cu-SAPO-18 sample showed a more significant loss in the SCR rate and its activation energy increased obviously from 30.5 to 45.1 kJ/mol, also in good consistence with NO conversion in the NH_3-SCR reaction. Therefore, compared with the catalysts with other lanthanide doping, Ce doping was conducive to improve the catalytic performance and hydrothermal aging stability.

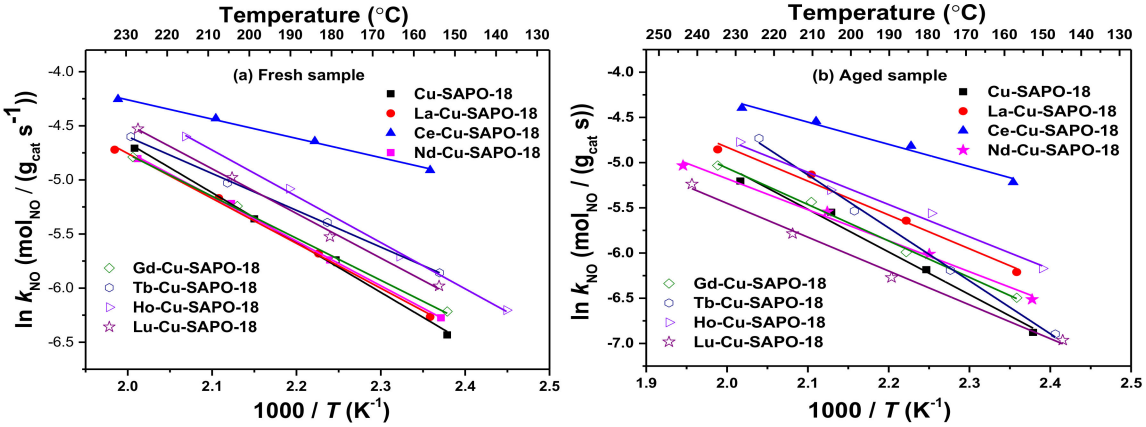

Figure 2. Arrhenius plots for the NH_3-SCR reaction in the low-temperature range over the (**a**) fresh and (**b**) hydrothermally aged Cu-SAPO-18 and M-Cu-SAPO-18 samples, at a GHVS of 800,000 h^{-1}. The reactant feed composition: 500 ppm NO, 500 ppm NH_3, 5 vol % H_2O, 14 vol % O_2, and N_2 (balance).

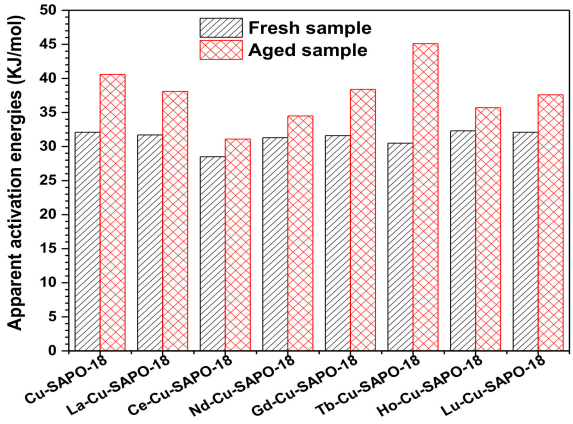

Figure 3. Apparent activation energies for the NH_3−SCR reaction over the fresh and hydrothermally aged Cu-SAPO-18 and M-Cu-SAPO-18 samples.

2.2. NH_3 Oxidation

The oxidation of NH_3 is the main competitive reaction because it reduces the reduction of NO_x. High-temperature SCR activity is closely related to the ammoxidation by O_2. In order to confirm the product of NH_3 oxidation in the NH_3-SCR reaction, NH_3 oxidation experiments were carried out over the Cu-SAPO-18 and M-Cu-SAPO-18 catalysts before and after hydrothermal aging treatment.

Figure 4a presents the catalytic activities of NH_3 oxidation over the fresh catalysts. NH_3 began to oxidize at 300 °C, and became more and more severe with increasing the temperature. There was a different change trend in catalytic activity of Cu-SAPO-18 and M-Cu-SAPO-18 for NH_3 oxidation. For instance, compared with the fresh Cu-SAPO-18 sample, NH_3 conversion decreased from 79.6% over Cu-SAPO-18 to 58.1% over Ce-Cu-SAPO-18 at 600 °C. These results suggest that Ce doping could inhibit the oxidation of NH_3. The decreases in NH_3 conversion and NO_x selectivity in NH_3 oxidation explain why the NO conversion over Ce-Cu-SAPO-18 increased at higher temperatures.

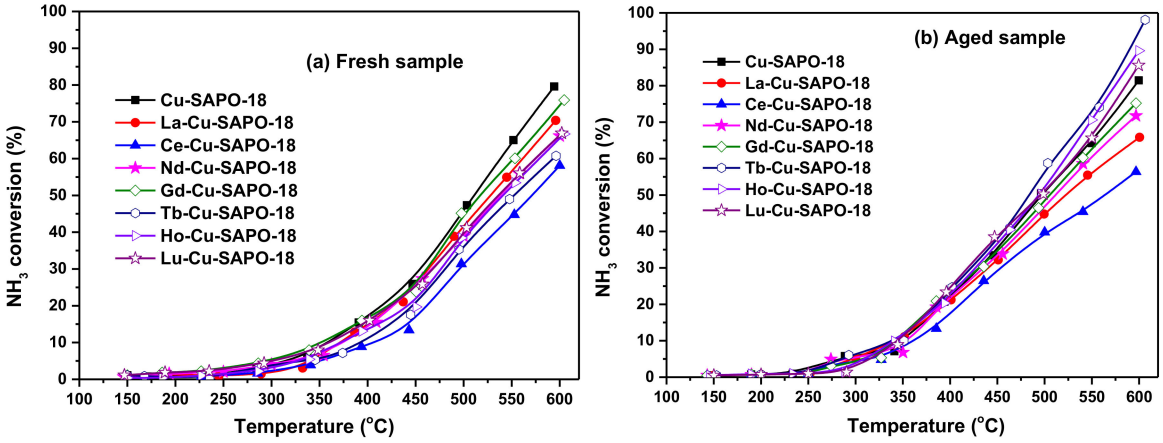

Figure 4. Catalytic activities for NH_3 oxidation over the (**a**) fresh and (**b**) hydrothermally aged Cu-SAPO-18 and M-Cu-SAPO-18 samples at a GHVS of 130,000 h^{-1}. The reactant feed composition: 500 ppm NH_3, 14 vol % O_2, and N_2 (balance).

Figure 4b shows the catalytic activities of NH_3 oxidation over the hydrothermally aged catalysts. Compared with their fresh counterparts, the Lu-Cu-SAPO-18-aged, Ho-Cu-SAPO-18-aged, and Tb-Cu-SAPO-18-aged samples showed increased NH_3 conversions and NO_x selectivity. This increase might be due to partial lattice damage and conversion of the copper site to an oxidized form, as evidenced by the following H_2-TPR results. Over Ce-Cu-SAPO-18-aged, however, NH_3 conversion and NO_x selectivity in NH_3 oxidation were not obviously changed. Actually, NH_3 conversion exhibited a slight decrease from 58.1% over fresh Ce-Cu-SAPO-18 to 56.4 % over Ce-Cu-SAPO-18-aged at 600 °C, and the extent of such a change was much less than those over the other samples. Therefore, the changes in NH_3 conversion and NO_x selectivity during NH_3 oxidation well explain the reason why the catalytic activity over Ce-Cu-SAPO-18 was higher than that over Cu-SAPO-18, even after the sample was hydrothermally aged.

2.3. Characterization of the Fresh and Aged Cu-SAPO-18 and M-Cu-SAPO-18 Catalysts

2.3.1. XRD and BET Results

Figure 5 shows XRD patterns of the fresh and aged M-Cu-SAPO-18 samples. As shown in Figure 5a, the fresh M-Cu-SAPO-18 samples displayed the typical XRD pattern of zeolite with an AEI framework [19], indicating that the structure was not destroyed after the adding of copper and lanthanide elements. Furthermore, there were no distinct differences in XRD pattern of the Cu-SAPO-18 and M-Cu-SAPO-18 samples.

Figure 5b shows XRD patterns of the Cu-SAPO-18-aged and M-Cu-SAPO-18-aged samples. Compared with the fresh samples, there was a change in diffraction peak intensity of the hydrothermally aged samples, demonstrating a difference in the collapse extent of the zeolitic crystal structure after the hydrothermal aging treatment. From Figure 5a,b, one can see that the structure was maintained in the Ce-Cu-SAPO-18-aged and La-Cu-SAPO-18-aged catalysts. However, the crystallinity of M-Cu-SAPO-18 (M = Nd, Ho, Lu or Gd) decreased slightly, which might be due to partial damage of the zeolite structure

due to the hydrothermal aging treatment. For the Tb-Cu-SAPO-18-aged sample, the hydrothermal aging treatment caused more serious damage of the SAPO-18 crystal structure.

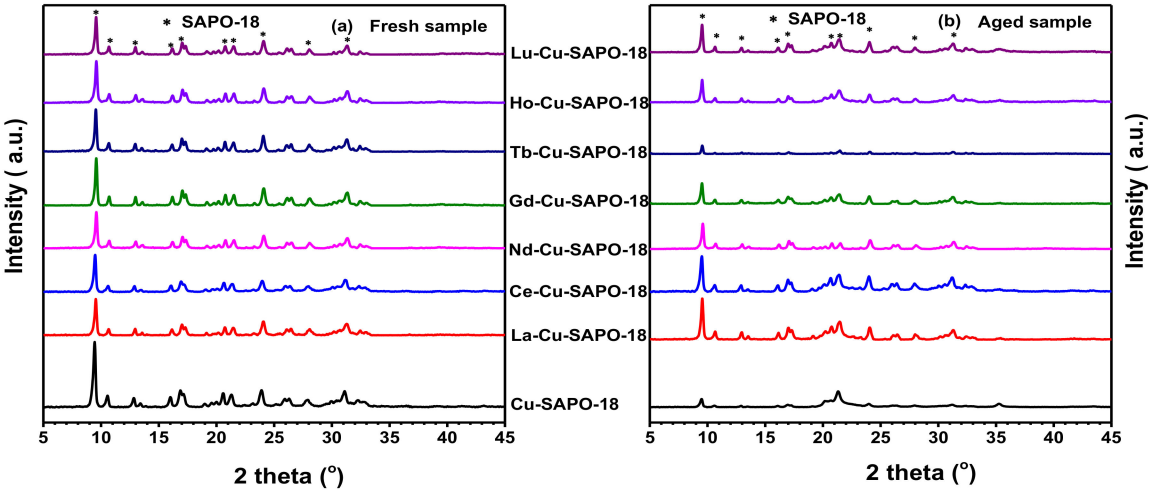

Figure 5. XRD patterns of the (**a**) fresh and (**b**) hydrothermally aged Cu-SAPO-18 and M-Cu-SAPO-18 samples.

BET surface areas and micropore volumes of the samples are summarized in Table 1. Surface area and micropore volume did not change much after loading the lanthanides on the Cu-SAPO-18 support, which was consistent with the XRD results. This result indicates that loading of the lanthanides had little effect on the structure of Cu-SAPO-18. After hydrothermal aging, surface areas and micropore volumes of all the samples decreased to various degrees, which indicates that the structure of these samples collapsed differently. Among them, the Ce-Cu-SAPO-18 samples did not decrease significantly, and surface area and micropore volume decreased by 11.92 and 15.02%, respectively.

Table 1. Chemical Compositions and BET Surface Areas of the Cu-SAPO-18 and M-Cu-SAPO-18 Samples.

Sample	Cu (wt %)	Lanthanide (wt %)	Al (wt %)	P (wt %)	Si (wt %)	S_{BET} (m^2/g)	Micropore Volume (cm^3/g)
Cu-SAPO-18	1.76	-	31.57	53.19	10.63	597	0.234
Cu-SAPO-18-aged	1.76	-	31.57	53.19	10.63	304	0.129
La-Cu-SAPO-18	1.69	1.27	30.80	53.62	8.95	563	0.229
La-Cu-SAPO-18-aged	1.69	1.27	30.80	53.62	8.95	428	0.178
Ce-Cu-SAPO-18	1.71	1.24	29.62	53.94	10.56	579	0.233
Ce-Cu-SAPO-18-aged	1.71	1.24	29.62	53.94	10.56	510	0.198
Nd-Cu-SAPO-18	1.68	1.35	30.05	52.80	8.93	559	0.228
Nd-Cu-SAPO-18-aged	1.68	1.35	30.05	52.80	8.93	421	0.177
Gd-Cu-SAPO-18	1.57	1.36	29.76	51.56	9.29	561	0.229
Gd-Cu-SAPO-18-aged	1.57	1.36	29.76	51.56	9.29	366	0.144
Tb-Cu-SAPO-18	1.65	1.18	29.52	52.16	8.80	569	0.230
Tb-Cu-SAPO-18-aged	1.65	1.18	29.52	52.16	8.80	358	0.142
Ho-Cu-SAPO-18	1.55	1.18	29.92	51.58	8.42	556	0.228
Ho-Cu-SAPO-18-aged	1.55	1.31	29.92	51.58	8.42	410	0.174
Lu-Cu-SAPO-18	1.69	1.28	27.81	48.47	9.03	543	0.224
Lu-Cu-SAPO-18-aged	1.69	1.28	27.81	48.47	9.03	415	0.175

2.3.2. XPS Results

The types of copper species on the catalyst surface were detected using the XPS technique [20]. Figure 6 illustrates Cu $2p_{3/2}$ XPS spectra of the fresh Cu-SAPO-18 and M-Cu-SAPO-18 catalysts. Each XPS spectrum shows two asymmetric signals that could be divided into three components at binding energies (BEs) of 932.6–933, 934.6–936.5, and 945.67–947.7 eV. According to the literature [20], the component at BE = 932.6–933 eV was assigned to the surface CuO species [21], while the one at

BE = 934.6–936.5 eV corresponded to the surface isolated Cu^{2+} ions, and the peak at BE = 945.67–947.7 eV was due to the shake-up satellite of the surface Cu^{2+} species on the fresh catalyst [22]. The Cu^{+} species were not detected by the XPS technique, which might be owing to the lower Cu^{+} content in the catalyst or the lower detection sensitivity of the XPS technique. The curve-fitting peaks of fresh Cu-SAPO-18 and M-Cu-SAPO-18 and their surface Cu species contents are shown in Figure 6 and Table 2, respectively. The surface Cu^{2+}/Cu_{surf} molar ratio ("Cu^{2+}" represents the content of isolated Cu^{2+} sites (i.e., in ion exchange positions of the zeolite structure) on the sample surface calculated from the XPS results, while "Cu_{surf}" represents the total copper content on the sample surface) decreased in the sequence of Ce-Cu-SAPO-18 (0.333) > Tb-Cu-SAPO-18 (0.298) > Gd-Cu-SAPO-18 (0.278) > La-Cu-SAPO-18 (0.276) > Cu-SAPO-18 (0.238) > Ho-Cu-SAPO-18 (0.235) > Nd-Cu-SAPO-18 (0.230) > Lu-Cu-SAPO-18 (0.225). Compared with the fresh Cu-SAPO-18 sample, the Cu^{2+}/Cu_{surf} molar ratio changed after the doping of lanthanide elements. For example, the surface Cu^{2+}/Cu_{surf} molar ratio increased after the doping of Ce, Tb, Gd or La, which was attributed to the synergistic effect of the lanthanide element and Cu species in the AEI-structured zeolitic skeleton [23]. The Cu^{2+}/Cu_{surf} molar ratio, however, decreased after Ho, Nd or Lu doping, which was due to the fact that the doping of such lanthanide elements might block the zeolite channels and/or occupy the active Cu^{2+} sites. Among the M-Cu-SAPO-18 samples, the highest surface Cu^{2+}/Cu_{surf} molar ratio (0.333) was achieved on Ce-Cu-SAPO-18. Therefore, after adding cerium, activity of the catalyst was improved. This result was due to synergistic effect of the cerium and copper species, which increased the separated copper ions, thereby enhancing the catalytic activity.

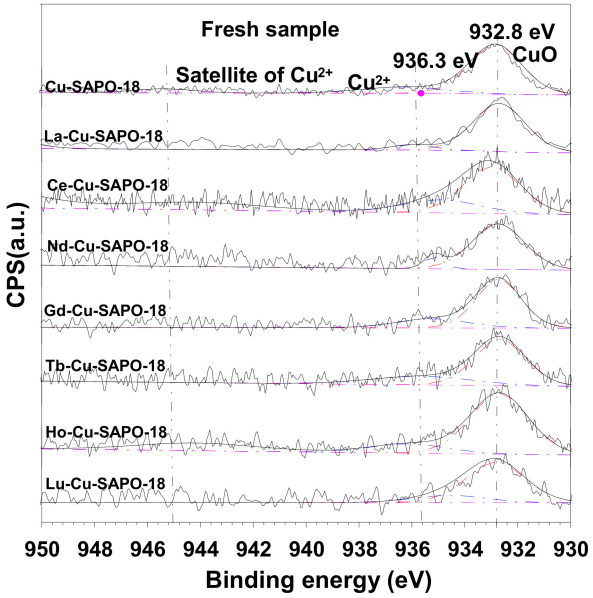

Figure 6. Cu $2p_{3/2}$ XPS spectra of the fresh Cu-SAPO-18 and M-Cu-SAPO-18 samples.

Figure 7 and Table 2 show the curve-fitting peaks and surface copper contents of the hydrothermally aged Cu-SAPO-18 and M-Cu-SAPO-18. The Cu^{2+}/Cu_{surf} molar ratio decreased according to the following order: Ce-Cu-SAPO-18-aged (0.275) > Gd-Cu-SAPO-18-aged (0.185) > Nd-Cu-SAPO-18-aged (0.178) > La-Cu-SAPO-18- aged (0.175) > Cu-SAPO-18-aged (0.161) > Lu-Cu-SAPO-18-aged (0.132) > Ho-Cu-SAPO-18-aged (0.128) > Tb-Cu-SAPO-18-aged (0.126). Compared with their fresh counterparts, surface Cu^{2+}/Cu_{surf} molar ratio of the hydrothermally aged samples changed in different extents.

For example, the Cu^{2+}/Cu_{surf} molar ratio decreased from 0.333 on Ce-Cu-SAPO-18 to 0.275 on Ce-Cu-SAPO-18-aged, which shows the lowest decrease in surface Cu^{2+}/Cu_{surf} molar ratio among all of the samples before and after hydrothermal aging treatment. The surface Cu^{2+}/Cu_{surf} molar ratio greatly decreased from 0.298 on Tb-Cu-SAPO-18 to 0.126 on Tb-Cu-SAPO-18-aged, which shows the highest decrease in surface Cu^{2+}/Cu_{surf} molar ratio of all of the samples before and after hydrothermal

aging treatment. Therefore, the Ce-Cu-SAPO-18 sample possessed the most stable surface Cu^{2+}/Cu_{surf} molar ratio either before or after hydrothermal aging treatment, which was also in agreement with the H_2-TPR results (shown below).

Table 2. $Cu2p_{3/2}$ XPS Curve-Fitting Results on the Surface of Cu-SAPO-18 and M-Cu-SAPO-18 Samples Before and After Hydrothermal Aged Treatment.

Sample	Isolated Cu^{2+} (mmol/g)	CuO (mmol/g)	Cu_{surf} (mmol/g)	Cu^{2+}/Cu_{surf} Molar Ratio
Cu-SAPO-18	0.0248	0.0900	0.1044	0.238
Cu-SAPO-18-aged	0.0131	0.0670	0.0812	0.161
La-Cu-SAPO-18	0.0456	0.1360	0.1651	0.276
La-Cu-SAPO-18-aged	0.0390	0.1950	0.2230	0.175
Ce-Cu-SAPO-18	0.0841	0.1685	0.2525	0.333
Ce-Cu-SAPO-18-aged	0.0674	0.1778	0.2452	0.275
Nd-Cu-SAPO-18	0.0460	0.1740	0.2000	0.230
Nd-Cu-SAPO-18-aged	0.0325	0.1489	0.1828	0.178
Gd-Cu-SAPO-18	0.0520	0.1444	0.1870	0.278
Gd-Cu-SAPO-18-aged	0.0401	0.1892	0.2169	0.185
Tb-Cu-SAPO-18	0.0638	0.1564	0.2142	0.298
Tb-Cu-SAPO-18-aged	0.0273	0.1880	0.2167	0.126
Ho-Cu-SAPO-18	0.0563	0.1994	0.2394	0.235
Ho-Cu-SAPO-18-aged	0.0228	0.1540	0.1783	0.128
Lu-Cu-SAPO-18	0.0414	0.1690	0.1840	0.225
Lu-Cu-SAPO-18-aged	0.0249	0.1586	0.1890	0.132

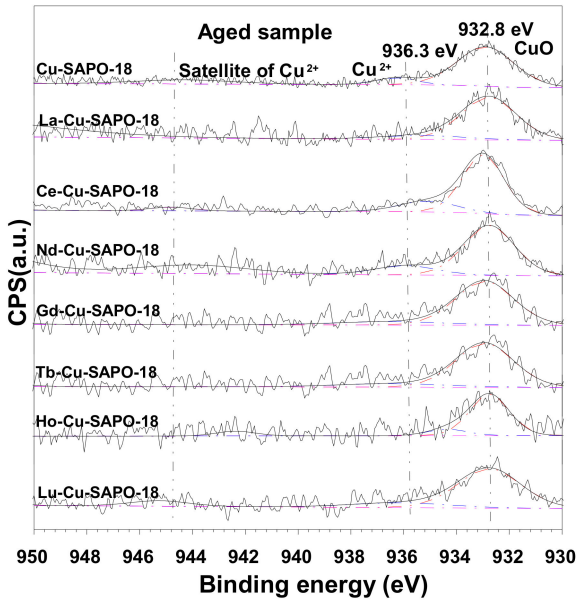

Figure 7. Cu $2p_{3/2}$ XPS spectra of the hydrothermally aged Cu-SAPO-18 and M-Cu-SAPO-18 samples.

Accordingly, a decrease in the surface Cu^{2+}/Cu_{surf} molar ratio indicates that Cu underwent transformation or migration on the surface of the skeleton due to the hydrothermal aging treatment. After introduction of Ce, hydrothermal stability of the catalyst was improved. This result was due to the synergistic effect of Ce and Cu in the AEI framework [23] that resulted in stabilization of the active centers and maintained activity of the catalyst.

2.3.3. H_2-TPR Results

H_2-TPR was performed to test interaction of the Cu and lanthanide elements. H_2-TPR profiles of all the samples are shown in Figures 8 and 9. Fresh samples displayed four reduction peaks. There

were three reduction peaks below 500 °C, indicating that there were three types of Cu species in the sample. According to the literature [24], the reduction peak (α) at low temperature was attributed to reduction of the isolated Cu^{2+} ions in the 8MRs cage, which was related to the NH_3-SCR reaction at low temperatures. The reduction peak at mid-temperature (β) corresponded to reduction of the CuO to Cu^0 [25]. The peak (γ) at higher temperatures was considered as reduction of the Cu^{2+} ions in the D6R cage [24], which was closely related to the activities in the mid-high temperature range.

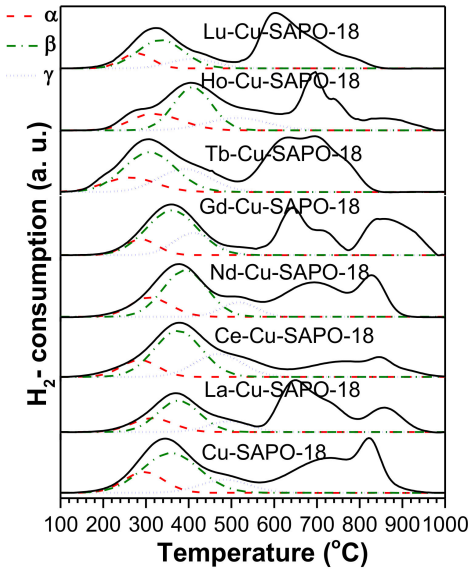

Figure 8. H_2-TPR profiles of the fresh samples.

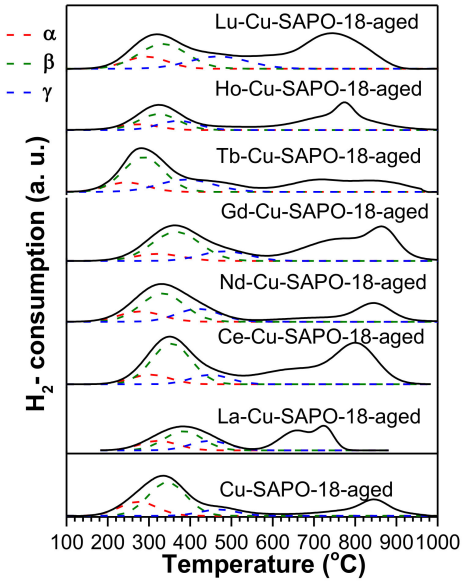

Figure 9. H_2-TPR profiles of the aged samples.

After adding the lanthanide, the γ peak below 600 °C in intenisty increased and the reduction peaks above 600 °C changed as compared with the Cu-SAPO-18 catalyst. To confirm the assignments of the reduction peaks, the free-Cu M-SAPO-18 catalysts were characterized by the H_2-TPR technique (Figure S2). The results show that the reduction peak temperatures of all of the M-SAPO-18 samples were higher than 600 °C, which was consistent with the results reported earlier [25]. Combining the H_2-TPR results of the above M-SAPO-18 and Cu-SAPO-18 samples, one can realize that the γ peak below 600 °C did not include reduction of the M element, which was consistent with the result reported

in the literature [26]. Therefore, it is inferred that the increase in γ peak area of the M-Cu-SAPO-18 catalysts was only attributed to the increase in isolated Cu^{2+} content in the D6R cage [27,28] after adding M element.

The estimated amounts of the copper species are summarized in Table 3. For the fresh samples, the content of total isolated Cu^{2+} ions decreased in the following order: Ce-Cu-SAPO-18 (108.7 umol/g) > Tb-Cu-SAPO-18 (102.5 μmol/g) > Gd-Cu- SAPO-18 (100.6 μmol/g) > La-Cu-SAPO-18 (99.9 μmol/g) > Cu-SAPO-18 (98.3 μmol/g) > Ho-Cu-SAPO-18 (98 μmol/g) > Nd-Cu-SAPO-18 (96.6 μmol/g) > Lu-Cu-SAPO-18 (81.4 μmol/g), which was in good consistence with the results of XPS.

Table 3. Quantitative Analysis on the H_2-TPR Profiles of the Samples.

Sample	Isolated Cu^{2+} (μmol/g)		Total Cu^{2+} (μmol/g)	CuO (μmol/g)
	8MRs	D6R		
Cu-SAPO-18	51.1	47.2	98.3	116.3
Cu-SAPO-18-aged	33.9	36.7	70.6	156.9
La-Cu-SAPO-18	46.8	53.1	99.9	112.4
La-Cu-SAPO-18-aged	39.4	42.2	81.6	140.8
Ce-Cu-SAPO-18	41.1	67.6	108.7	93.0
Ce-Cu-SAPO-18-aged	38.0	65.5	103.5	100.5
Nd-Cu-SAPO-18	46.2	50.4	96.6	115.1
Nd-Cu-SAPO-18-aged	41.7	39.4	81.1	136.1
Gd-Cu-SAPO-18	34.5	66.1	100.6	105.1
Gd-Cu-SAPO-18-aged	33.0	52.7	85.7	140.0
Tb-Cu-SAPO-18	60.3	42.2	102.5	103.8
Tb-Cu-SAPO-18-aged	26.4	23.5	49.9	176.4
Ho-Cu-SAPO-18	55.0	43.0	98	106.5
Ho-Cu-SAPO-18-aged	32.7	35.5	68.2	166.7
Lu-Cu-SAPO-18	47.8	33.6	81.4	126.9
Lu-Cu-SAPO-18-aged	28.2	19.9	48.1	148.1

However, amount of the isolated Cu^{2+} species in the D6R cage decreased in the sequence: Ce-Cu-SAPO-18 (67.6 μmol/g) > Gd-Cu-SAPO-18 (66.1 μmol/g) > La-Cu-SAPO-18 (53.1 μmol/g) > Nd-Cu-SAPO-18 (50.4 μmol/g) > Cu-SAPO-18 (47.2 μmol/g) > Ho-Cu-SAPO-18 (43.0 μmol/g) > Tb-Cu-SAPO-18 (42.2 μmol/g) > Lu-Cu-SAPO-18 (33.6 μmol/g). Compared with the fresh Cu-SAPO-18 sample, amount of the isolated Cu^{2+} species in the D6R cage increased after the doping of Ce, Gd, La or Nd, whereas it decreased after the doping of Ho, Tb or Lu. For example, amount of the isolated Cu^{2+} species in the D6R cage increased from 47.2 μmol/g in Cu-SAPO-18 to 67.6 μmol/g in Ce-Cu-SAPO-18, but that in the 8MRs cage decreased from 51.1 μmol/g in Cu-SAPO-18 to 41.1 μmol/g in Ce-Cu-SAPO-18. On the contrary, amount of the isolated Cu^{2+} species in the D6R cage decreased from 47.2 μmol/g in Cu-SAPO-18 to 42.2 μmol/g in Tb-Cu-SAPO-18, and that in the 8MRs cage increased from 51.1 μmol/g in Cu- SAPO-18 to 60.3 μmol/g in Tb-Cu-SAPO-18. The results indicate that the Ce-doped sample was conducive to incorporation of the Cu species to the D6R sites of SAPO-18, and the Tb-doped sample promoted the Cu species to enter the 8MRs cage of SAPO-18. The results of our previous work [29] showed that stability of the isolated Cu^{2+} species in the D6R cage was better than that of the isolated Cu^{2+} species in the 8MRs cage. The addition of Ce not only increased overall amount of the isolated Cu^{2+} species, but also improved stability of Ce-Cu-SAPO-18.

H_2-TPR profiles and amounts of the copper species after the hydrothermal aged treatment are also shown in Figure 9 and Table 3, respectively. It can be seen that there were some differences in Cu species of the samples before and after hydrothermal aging treatment. Amount of the total isolated Cu^{2+} ions decreased in the following order: Ce-Cu-SAPO-18-aged (103.5 μmol/g) > Gd-Cu-SAPO-18-aged (85.7 μmol/g) > La-Cu-SAPO-18-aged (81.6 μmol/g) > Nd-Cu-SAPO-18-aged (81.1 μmol/g) > Cu-SAPO-18-aged (70.6 μmol/g) > Ho-Cu-SAPO-18-aged (68.2 μmol/g) > Tb-Cu-SAPO-18-aged (49.9 μmol/g) > Lu-Cu-SAPO-18-aged (48.1 μmol/g), which was in good agreement with the sequence in amount of the isolated Cu^{2+} species in the D6R cage of the fresh samples. The results confirm that the

more the isolated Cu^{2+} species amount in the D6R cage, the more stable was the sample [29]. Furthermore, as compared with Cu-SAPO-18, the Ce-Cu-SAPO-18, Gd-Cu-SAPO-18, La-Cu- SAPO-18, and Nd-Cu-SAPO-18 samples contained more amounts of the isolated Cu^{2+} species in the D6R cage, resulting in a better hydrothermal aging performance than the Cu-SAPO-18 sample. On the contrary, for the Ho-Cu-SAPO-18, Tb-Cu-SAPO-18, and Lu-Cu-SAPO-18 samples, more amounts of the isolated Cu^{2+} species in the 8MRs cage (Table 3) led to the poor hydrothermal aging performance. Particularly, for Ce-Cu-SAPO-18, the isolated Cu^{2+} species amount decreased slightly from 108.7 umol/g in Ce-Cu-SAPO-18 to 103.5 μmol/g in Ce-Cu-SAPO-18-aged, which was the lowest loss in amount of the isolated Cu^{2+} species in all of the samples. The amount of the isolated Cu^{2+} species, however, decreased significantly from 102.5 μmol/g in Tb-Cu-SAPO-18 to 49.9 μmol/g in Tb-Cu-SAPO-18-aged. It again confirms that Ce-Cu-SAPO-18 had the most stable isolated Cu^{2+} species amount either before or after hydrothermal aging treatment, which were in good consistence with the results of XPS characterization.

2.3.4. NMR Results

Solid-state NMR technique was used to study the changes in skeleton structure of the samples before and after hydrothermal aging treatment. ^{27}Al solid-state NMR spectrum of a zeolitic sample can provide information related to coordination states of the Al species in the sample. From Figure 1, it can be seen that catalytic activities over the Tb-Cu-SAPO-18 samples before and after hydrothermal aging treatment were quite different, but those over the fresh and hydrothermally aged Ce-Cu-SAPO-18 samples remained almost unchanged. In order to explore the changes in zeolitic skeleton structure, ^{27}Al MAS NMR characterization of the Cu-SAPO-18, Ce-Cu-SAPO-18, and Tb-Cu-SAPO-18 samples before and after hydrothermal aging treatment was performed, and their spectra are shown in Figure 10. For the SAPO-18 sample, the featured signal at 38 ppm was attributed to the framework of tetrahedral Al (Al_f) [30], whereas the one at −7 ppm was ascribed to the extra-framework of octahedral Al [31]. As shown in Figure 10, only a small amount of extra-framework Al atoms were detected, while almost all of the Al atoms stayed as Al_f in the fresh samples. After hydrothermal aging treatment, intensity of the signal at 38 ppm decreased significantly in the Cu-SAPO-18 and Tb-Cu-SAPO-18 samples. Compared with Cu-SAPO-18 (decrease by 35.1%), Tb-Cu-SAPO-18 (decrease by 66.8 %) showed a more obvious Al_f loss after hydrothermal treatment. In contrast, there was slight change (decrease by 4.1%) in peak intensity of Ce-Cu-SAPO-18. The change in hydrothermal stability of the sample was observed to be consistent with the alteration in SCR activity. Obviously, these results confirm that Ce doping could stabilize the framework Al in the Al-rich Cu-SAPO-18 sample.

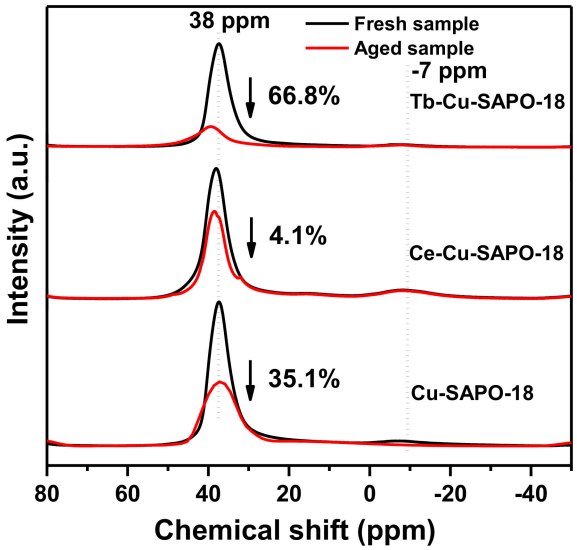

Figure 10. ^{27}Al NMR spectra of before (black line) and after (red line) hydrothermally aged Cu-SAPO-18 and M-Cu-SAPO-18 (M = Ce or Tb).

2.3.5. NH_3-TPD Results

Acidity is an important parameter related to NH_3-SCR activity of a catalyst. The activation and adsorption of NH_3 is often used to determine the acid center of the zeolitic material [32]. Although acidic sites were not the decisive factors affecting catalytic activity, it could indirectly help us to elucidate properties of the catalysts. Figure 11 shows NH_3-TPD profiles of the fresh and hydrothermally aged Cu-SAPO-18 and M-Cu-SAPO-18 catalysts. In the fresh samples, there were three peaks at 200, 350, and 500 °C. According to the literature [29,33], the desorption peak at 200 °C was ascribed to physical adsorption of the NH_3 or adsorption of the NH_3 on the surface hydroxyl group (Si–OH, P–OH or Al–OH), the one at 350 °C was a strong Lewis acid site produced by the Cu^{2+} ion exchange [34], and the one at above 500 °C was due to adsorption of the NH_3 on the structural Brønsted acid sites with moderately strong acidity. The acid amount of the catalyst was obtained by curve-fitting of the NH_3-TPD profiles, as shown in Table 4. Amount of the total acid sites decreased in the order of Cu-SAPO-18 (0.634 mmol/g) > Ce-Cu-SAPO-18 (0.584 mmol/g) > Tb-Cu-SAPO-18 (0.508 mmol/g) > Gd-Cu-SAPO-18 (0.499 mmol/g) > La-Cu-SAPO-18 (0.489 mmol/g)> Ho-Cu-SAPO-18 (0.476 mmol/g) > Lu-Cu-SAPO-18 (0.473 mmol/g) > Nd-Cu-SAPO-18 (0.467 mmol/g). The total acid quantity of the fresh M-Cu-SAPO-18 samples showed a decreasing trend, which might be due to the fact that the lanthanide element substituted the H^+ in −Si−O(H)−Al and reduced acidity of the catalyst or partial metal species were enriched by covering the acid sites [18]. When Lu was added to Cu-SAPO-18, however, amount of the total acid sites decreased most obviously from 0.634 mmol/g in Cu-SAPO-18 to 0.473 mmol/g in Lu-Cu-SAPO-18. Meanwhile, amount of the acid sites decreased only slightly from 0.634 mmol/g in Cu-SAPO-18 to 0.584 mmol/g in Ce-Cu-SAPO-18. Additionally, amount of the Lewis acid sites increased slightly from 0.101 mmol/g in Cu-SAPO-18 to 0.159 mmol/g in Ce-Cu-SAPO-18, indicating that the more abundant isolated Cu^{2+} species existed in Ce-Cu-SAPO-18, which was in good agreement with the XPS and TPR characterization results. The changes in amount of the moderate acid sites might be related to the Ce- and Cu-doping effect. Figure 11 shows NH_3-TPD profiles of the M-Cu-SAPO-18-aged samples. After hydrothermal aging treatment, intensity of the NH_3 desorption peaks of the M-Cu-SAPO-18-aged and Cu-SAPO-18-aged samples was reduced, as compared with that of their fresh counterparts, indicating that amounts of the Lewis acid sites and Brønsted acid sites decreased after hydrothermal aging treatment. The reduction in the number of acid centers might be due to partial destruction of the zeolitic structure (^{27}Al NMR results (Figure 10)) and a decrease in the number of the active Cu^{2+} species in the sample (H_2-TPR results (Figures 8 and 9 and Table 3)). As shown in Table 4, amount of the total acid sites decreased in the order of Ce-Cu-SAPO-18-aged (0.535 mmol/g) > Gd-Cu-SAPO-18-aged (0.458 mmol/g) > La-Cu-SAPO-18-aged (0.443 mmol/g) > Nd-Cu-SAPO-18-aged (0.386 mmol/g) > Cu-SAPO-18-aged (0.381 mmol/g) > Ho-Cu-SAPO-18-aged (0.375 mmol/g) > Tb-Cu-SAPO-18-aged (0.354 mmol/g) > Lu-Cu-SAPO-18-aged (0.348 mmol/g). The decrease in total acid amount was related to structure destruction of the sample and decrease in content of the isolated Cu^{2+} ions. By comparing the fresh Cu-SAPO-18 and Ce-Cu-SAPO-18 catalysts, the influence of hydrothermal aging treatment on acid amount of Ce-Cu-SAPO-18 was relatively small, and amount of the acid sites decreased slightly from 0.584 mmol/g in Ce-Cu-SAPO-18 to 0.535 mmol/g in Ce-Cu-SAPO-18-aged. Furthermore, the most prominent difference was that the amount of the NH_3 desorbed from the Brønsted acid sites in all of the hydrothermally aged samples above 500 °C decreased considerably. In particular, the NH_3 desorption above 500 °C was still observed from the hydrothermally aged Ce-Cu-SAPO-18 sample. The acid quantity of NH_3 desorption above 500 °C of Ce-Cu-SAPO-18-aged was found to be approximately 0.301 mmol/g, corresponding to 94.7% of acid quantity of NH_3 desorption above 500 °C (0.318 mmol/g) of Ce-Cu-SAPO-18. For the other samples, high-temperature NH_3 desorption decreased obviously. The acid quantity of NH_3 desorption from the mental ions and other Lewis acid sites of Ce-Cu-SAPO-18-aged below 500 °C did not change significantly, as compared with that of Ce-Cu-SAPO-18. In particular, the Ce-Cu-SAPO-18-aged sample possessed a higher ammonia storage capacity than the other aged samples.

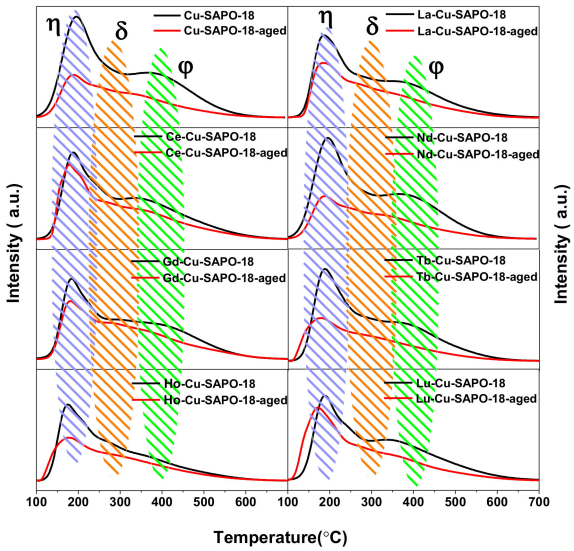

Figure 11. NH_3-TPD profiles of the fresh and hydrothermally aged Cu-SAPO-18 and M-CuSAPO-18 samples.

Table 4. Acidity of the Samples Obtained from Their NH_3-TPD Profiles.

Sample	Acidity (mmol/g)			Amount (mmol/g)
	Weak	Moderate	Strong	
Cu-SAPO-18	0.204	0.101	0.329	0.634
Cu-SAPO-18-aged	0.071	0.086	0.224	0.381
La-Cu-SAPO-18	0.082	0.085	0.322	0.489
La-Cu-SAPO-18-aged	0.070	0.074	0.289	0.443
Ce-Cu-SAPO-18	0.107	0.159	0.318	0.584
Ce-Cu-SAPO-18-aged	0.143	0.091	0.301	0.535
Nd-Cu-SAPO-18	0.097	0.090	0.280	0.467
Nd-Cu-SAPO-18-aged	0.079	0.065	0.242	0.386
Gd-Cu-SAPO-18	0.084	0.089	0.326	0.499
Gd-Cu-SAPO-18-aged	0.073	0.086	0.299	0.458
Tb-Cu-SAPO-18	0.104	0.103	0.301	0.508
Tb-Cu-SAPO-18-aged	0.081	0.074	0.199	0.354
Ho-Cu-SAPO-18	0.091	0.092	0.293	0.476
Ho-Cu-SAPO-18-aged	0.080	0.084	0.211	0.375
Lu-Cu-SAPO-18	0.078	0.085	0.310	0.473
Lu-Cu-SAPO-18-aged	0.075	0.081	0.192	0.348

2.3.6. Reactivity of NH_3 Adsorption

The performance of the samples before and after hydrothermal aging can be verified by the NH_3 adsorption DRIFTS characterization. NH_3 was used as a probe molecule to estimate the acidity of a sample [35]. Ammonia can be adsorbed on the Lewis and Brønsted acid sites [33]. DRIFTS spectra of the samples are shown in Figures 12 and 13. For the fresh samples, there were the bands at 3671, 3625, and 3600 cm^{-1}, which were attributed to the OH species on the sample surface [30]. For example, the band at 3671 cm^{-1} was due to the NH_3 adsorbed on the P−OH sites [30,36], and the one at 3625 and 3600 cm^{-1} corresponded to the bending vibration of the Al−OH−Si bond [37,38], which was the feature of the Brønsted acid sites in the 8MRs cage [36]. As a solid sample, frequency of the OH stretching vibration is in the range of 3500−3300 cm^{-1}, while those after NH_3 adsorption appeared at 3600, 3625 and 3671 cm^{-1}. It shows that position of the peak really was shifted due to the interaction of NH_3, which was consistent with the results reported by Y. Li et al. [39]. Additionally, the bands at 3000−3400 cm^{-1} were attributed to the N−H bonds [30]. Figure 12 presents the corresponding internal asymmetric T−O−T vibration *vas*(T−O−T) of fresh samples. The *vas*(T−O−T) feature was

caused by disturbance of the Cu^{2+} ions near the frame. The band at 840 cm^{-1} was induced by the Cu^{2+} ions near to the D6R cage, while the band at 910 cm^{-1} was related to the Cu^{2+} ions near to the 8MR cage. Hun et al. [40] assigned the bands at 850 and 900 cm^{-1} to the Cu^{2+} in the D6R and CHA cages, respectively, and the low frequency broad band was caused by the different coordination environment of Cu^{2+}. The Cu and lanthanide contents in the samples are shown in Table 1. As compared with Cu-SAPO-18, the band at 859 cm^{-1} of Ce-Cu-SAPO-18 and Tb-Cu-SAPO-18 was strong in intensity and well-resolved (Figure 12), suggesting migration of the Cu^{2+} ions to the D6R faces, which was consistent with the H_2-TPR results (Figure 8). For the other six samples, the band at 840 cm^{-1} became much weaker in intensity and less resolved. Intensity of the band at 900 cm^{-1} increased with different extents for the six samples except the Ce-Cu-SAPO-18 sample, which might be due to increase of the Cu^{2+} content in the 8MRs cage after addition of the rare earth element.

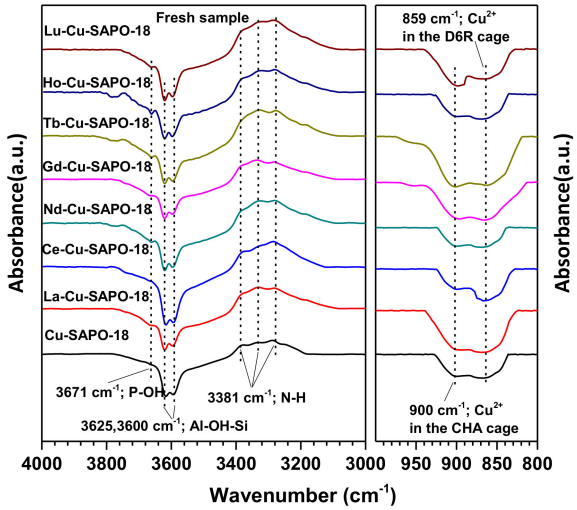

Figure 12. DRIFT spectra of NH_3 adsorbed on the fresh Cu-SAPO-18 and M-Cu-SAPO-18 samples. Experimental conditions: the sample was exposed to 500 ppm NH_3 (N_2 as the balance gas) at 30 °C for 1 h, and the total flow was 100 mL/min.

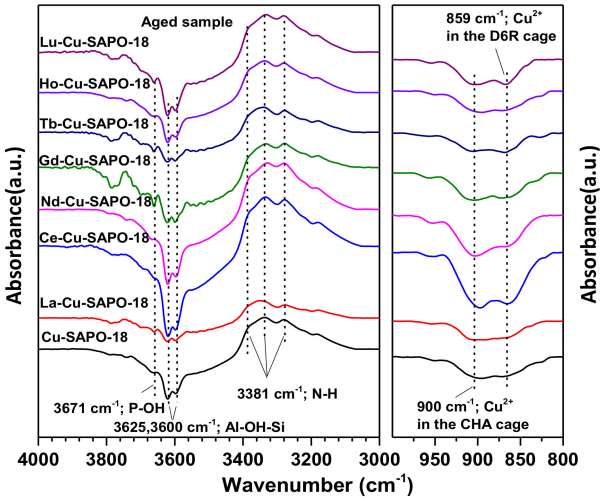

Figure 13. DRIFT spectra of NH_3 adsorbed on the hydrothermally aged Cu-SAPO-18 and M-Cu-SAPO-18 samples. Experimental conditions: the sample was exposed to 500 ppm NH_3 (N_2 as the balance gas) at 30 °C for 1 h, and the total flow was 100 mL/min.

Figure 13 shows DRIFTS spectra of NH_3 adsorption on the hydrothermally aged samples. The band intensity of NH_3 adsorption on the hydrothermally aged samples decreased with different extents,

which was consistent with the NH_3-TPD results (Figure 11 and Table 4). In particular, the OH and N−H tensile vibration of the Cu-SAPO-18 sample was significantly weakened, which was also attributed to the collapse of the zeolitic structure caused by the hydrothermal aging treatment. It can be seen that there were some differences in band intensity of the M-Cu-SAPO-18 samples before and after the hydrothermal aging treatment. For example, compared with the fresh Ce-Cu-SAPO-18 sample, intensity of the bands at 3671, 3625, and 3600 cm^{-1} of the Ce-Cu-SAPO-18-aged sample decreased slightly. In addition, the bands at 840 and 900 cm^{-1} became much weaker in intensity and less resolved, except for the Ce-Cu-SAPO-18-aged sample. The results demonstrate that after hydrothermal aging treatment, amount of the isolated Cu^{2+} species decreased in the AEI structure, in good consistence with the H_2-TPR results (Figure 9). At the same time, it also confirms that Ce adding enhanced the hydrothermal aging resistance of the Ce-Cu-SAPO-18 sample.

3. Experimental

3.1. Catalyst Preparation

N,*N*-diisopropyle-thylamine ($C_8H_{19}N$, DIPEA, Sinopharm Chemical Reagent Co., Ltd., Beijing, China) was used as the template. NH_4Cl (Sinopharm Chemical Reagent Co., Ltd., Beijing, China) aqueous solution and H-SAPO-18 precursor were mixed for ion exchange to obtain the NH_4/SAPO-18 sample. Afterwards, 1.0 g of NH_4/SAPO-18 was added to 60 mL of the mixed solution containing desired amounts of $Cu(NO_3)_2$ (Sinopharm Chemical Reagent Co., Ltd., Beijing, China) and $M(NO_3)_3$ (M = La, Ce, Nd, Gd, Tb, Ho or Lu) (Sinopharm Chemical Reagent Co., Ltd., Beijing, China) under stirring.

Then, the samples were dried in an oven at 120 °C for 12 h to remove residual water and calcined in an air flow (30 mL/min) at 500 °C for 6 h. In order to examine the hydrothermal stability, each of the M-Cu-SAPO-18 samples was treated in a 10% H_2O-containing air flow (300 mL/min) at 850 °C for 12 h. The detailed preparation procedures are described in the Supplementary Materials.

3.2. Catalyst Characterization

Physicochemical properties of the M-Cu-SAPO-18 samples were characterized by means of techniques, such as X-ray fluorescence spectrometer (XRF, Shimadzu, Kyoto, Japan), X-ray diffraction (XRD, Philips, Amsterdam, Netherlands), N_2 adsorption–desorption (BET, JWGB Sci & Tech Ltd., Beijing, China), X-ray photoelectron spectroscopy (XPS, Thermo Fisher Scientific, 81 Wyman Street, Waltham, MA, USA), hydrogen temperature-programmed reduction (H_2-TPR, Beijing Biod Electronic Technology Co., Ltd., Beijing, China), nuclear magnetic resonance (NMR, Agilent Technologies, Shanghai, China), ammonia temperature-programmed desorption (NH_3-TPD, Beijing Biod Electronic Technology Co., Ltd., Beijing, China), and in situ diffused reflectance infrared Fourier transform spectroscopy (in situ DRIFTS, Bruker, Karlsruhe, Germany). The detailed characterization procedures are stated in the Supplementary Materials.

3.3. Catalytic Evaluation

Catalytic activities of the samples were evaluated using a using a fixed-bed quartz tubular microreactor. The simulated exhaust gas consisted of 500 ppm NO, 500 ppm NH_3, 14 vol % O_2, 5 vol % H_2O, and N_2 (balance) with a total flow rate of 300 mL/min. The exhaust gas consisted of 500 ppm NH_3, 14 vol % O_2, 5 vol % H_2O, and N_2 (balance) for NH_3 oxidation. The detailed evaluation procedures are described in the Supplementary Materials.

4. Conclusions

The lanthanide (La, Ce, Nd, Gd, Tb, Ho or Lu)-doped Cu-SAPO-18 catalysts were prepared using the ion-exchange method. Doping of the lanthanide element influenced the zeolite structure and interactions between copper and lanthanide ions. The introduction of Ce to Cu-SAPO-18 weakened the interaction between Cu ions and AEI framework, which allowed the Cu ions to be positioned deeper

in the 8MRs cage and became more reducible. Ce doping promoted the Cu^{2+} species to migrate to the energetically favourable sites, whereas doping of the other lanthanide elements did not induce such a promotion effect on Cu ions migration. Additionally, Ce doping could improve hydrothermal stability of Cu-SAPO-18 by weakening hydrolysis of the zeolite structure during the hydrothermal aging treatment process. Furthermore, doping of Ce increased the catalytic activity at low and high temperatures, which was due to modification of the redox and/or isolated Cu^{2+} active sites. Therefore, it is concluded that introduction of Ce could improve catalytic activity and hydrothermal stability of the Cu-SAPO-18 sample, whereas doping of the other lanthanide elements did not exert such a positive effect on catalytic activity and hydrothermal stability.

Supplementary Materials: The following are available online at http://www.mdpi.com/2073-4344/10/3/336/s1, Catalyst preparation procedures, catalyst characterization, catalytic evaluation, discussion, Figure S1: NO conversion of the Cu-SAPO-18 and Ce-Cu-SAPO-18 catalysts at different calcination temperatures (500 and 600 °C). The reactant feed composition: 500 ppm NO + 500 ppm NH_3 + 14 vol % O_2 + 5 vol % H_2O + N_2 (balance); GHSV = 130,000 h^{-1}, Figure S2: H_2-TPR profiles of the M-SAPO-18 samples.

Author Contributions: Conceptualization, Q.Y.; Methodology, Q.G. and S.H.; Software, Q.G. and S.H.; Investigation, Q.G. and S.H.; Resources, Q.Y.; Data Curation, Q.G. and S.H.; Writing—Original Draft Preparation, Q.G.; Writing—Review & Editing, H.D.; Visualization, T.K. and S.C.; Supervision, Q.Y. and H.D.; Project Administration, Q.Y.; Funding Acquisition, Q.Y. All authors have read and agreed to the published version of the manuscript.

Funding: This work was supported by the National Natural Science Foundation of China (21277008 and 20777005), the National Key Research and Development Program of China (2017YFC0209905), and the Natural Science Foundation of Beijing (8082008). We also thank Ralph T. Yang (University of Michigan) for his helpful discussion and encouragement.

Conflicts of Interest: The authors declare no conflict of interest.

References

1. Matsumoto, K.; Tominaga, S.; Igawa, M. Measurements of atmospheric aerosols with diameters greater than 10 μm and their contribution to fixed nitrogen deposition in coastal urban environment. *Atmos. Environ.* **2011**, *45*, 6433–6438. [CrossRef]
2. Kim, M.J.; Park, R.J.; Kim, J. Urban air quality modeling with full O_3–NO_x–VOC chemistry: Implications for O_3 and PM air quality in a street canyon. *Atmos. Environ.* **2012**, *47*, 330–340. [CrossRef]
3. Shen, M.; Wen, H.; Hao, T.; Yu, T.; Fan, D.; Wang, J.; Li, W.; Wang, J. Deactivation mechanism of SO_2 on Cu/SAPO-34 NH_3-SCR catalysts: structure and active Cu^{2+}. *Catal. Sci. Technol.* **2015**, *5*, 1741–1749. [CrossRef]
4. Qi, G.; Yang, R.T.; Chang, R. MnO_x-CeO_2 mixed oxides prepared by co-precipitation for selective catalytic reduction of NO with NH_3 at low temperatures. *Appl. Catal. B Environ.* **2004**, *51*, 93–106. [CrossRef]
5. Praliaud, H.; Mikhailenko, S.; Chajar, Z.; Primet, M. Surface and bulk properties of Cu–ZSM-5 and Cu/Al_2O_3 solids during redox treatments. Correlation with the selective reduction of nitric oxide by hydrocarbons. *Appl. Catal. B Environ.* **1998**, *16*, 359–374. [CrossRef]
6. Bates, S.A.; Verma, A.A.; Paolucci, C.; Parekh, A.A.; Anggara, T.; Yezerets, A.; Schneider, W.F.; Miller, J.T.; Delgass, W.N.; Ribeiro, F.H. Identification of the active Cu site in standard selective catalytic reduction with ammonia on Cu-SSZ-13. *J. Catal.* **2014**, *312*, 87–97. [CrossRef]
7. Li, J.; Chang, H.; Ma, L.; Hao, J.; Yang, R.T. Low-temperature selective catalytic reduction of NO_x with NH_3 over metal oxide and zeolite catalysts—A review. *Catal. Today* **2011**, *175*, 147–156. [CrossRef]
8. Choo, S.T.; Yim, S.D.; Nam, I.; Ham, S.; Lee, J. Effect of promoters including WO_3 and BaO on the activity and durability of V_2O_5/sulfated TiO_2 catalyst for NO reduction by NH_3. *Appl. Catal. B Environ.* **2003**, *44*, 237–252. [CrossRef]
9. Fickel, D.W.; Addio, E.D.; Lauterbach, J.A.; Lobo, R.F. The ammonia selective catalytic reduction activity of copper-exchanged small-pore zeolites. *Appl. Catal. B Environ.* **2011**, *102*, 441–448. [CrossRef]
10. Sjövall, H.; Blint, R.J.; Olsson, L. Detailed kinetic modeling of NH_3 SCR over Cu-ZSM-5. *Appl. Catal. B Environ.* **2009**, *92*, 138–153. [CrossRef]

11. Mihai, O.; Widyastuti, C.R.; Andonova, S.; Kamasamudram, K.; Li, J.; Joshi, S.Y.; Currier, N.W.; Yezerets, A.; Olsson, L. The effect of Cu-loading on different reactions involved in NH_3-SCR over Cu-BEA catalysts. *J. Catal.* **2014**, *311*, 170–181. [CrossRef]
12. Iwamoto, M.; Furukawa, H.; Mine, Y.; Uemura, F.; Mikuriya, S.; Kagawa, S. Copper(II) ion-exchanged ZSM-5 zeolites as highly active catalysts for direct and continuous decomposition of nitrogen monoxide. *J. Chem. Soc. Chem. Commun.* **1986**, 1272–1273. [CrossRef]
13. Beale, A.M.; Gao, F.; Lezcano-Gonzalez, I.; Peden, C.H.; Szanyi, J. Recent advances in automotive catalysis for NO_x emission control by small-pore microporous materials. *Chem. Soc. Rev.* **2015**, *44*, 7371–7405. [CrossRef] [PubMed]
14. Schmieg, S.J.; Oh, S.H.; Kim, C.H.; Brown, D.B.; Lee, J.H.; Peden, C.H.F.; Kim, D.H. Thermal durability of Cu-CHA NH_3-SCR catalysts for diesel NO_x reduction. *Catal. Today* **2012**, *184*, 252–261. [CrossRef]
15. Ye, Q.; Wang, L.; Yang, R.T. Activity, propene poisoning resistance and hydrothermal stability of copper exchanged chabazite-like zeolite catalysts for SCR of NO with ammonia in comparison to Cu/ZSM-5. *Appl. Catal. A. Gen.* **2012**, *427–428*, 24–34. [CrossRef]
16. Martínez-Franco, R.; Moliner, M.; Corma, A. Direct synthesis design of Cu-SAPO-18, a very efficient catalyst for the SCR of NO_x. *J. Catal.* **2014**, *319*, 36–43. [CrossRef]
17. Bin, F.; Wei, X.; Li, B.; Hui, K.S. Self-sustained combustion of carbon monoxide promoted by the Cu-Ce/ZSM-5 catalyst in $CO/O_2/N_2$ atmosphere. *Appl. Catal. B Envivron.* **2015**, *162*, 282–288. [CrossRef]
18. Samojeden, B.; Teresa, G.; Kowal, J.; Szymaszek, A.; Jabłońska, M.; Gläser, R.; Motak, M. The influence of holmium on catalytic properties of Fe or Cu-modified vermiculites. *Physicochem. Probl. Mi.* **2019**, *55*, 1484–1495.
19. Chen, J.; Li, J.; Yuan, C.; Xu, S.; Wei, Y. Elucidating the olefin formation mechanism in the methanol to olefin reaction over AlPO-18 and SAPO-18. *Catal. Sci. Technol.* **2014**, *4*, 3268–3277. [CrossRef]
20. Wang, J.; Liu, Z.; Feng, G.; Chang, L.; Bao, W. In situ synthesis of CuSAPO-34/cordierite and its selective catalytic reduction of nitrogen oxides in vehicle exhaust: The effect of HF. *Fuel* **2013**, *109*, 101–109. [CrossRef]
21. Ghodselahi, T.; Vesaghi, M.A.; Shafiekhani, A.; Baghizadeh, A.; Lameii, M. XPS study of the $Cu@Cu_2O$ core-shell nanoparticles. *Appl. Surf. Sci.* **2008**, *255*, 2730–2734. [CrossRef]
22. Han, S.; Ye, Q.; Cheng, S.; Kang, T.; Dai, H. Effect of the hydrothermal aging temperature and Cu/Al ratio on the hydrothermal stability of CuSSZ-13 catalysts for NH_3-SCR. *Catal. Sci. Technol.* **2017**, *7*, 703–717. [CrossRef]
23. Wang, J.; Peng, Z.; Qiao, H.; Yu, H.; Hu, Y.; Chang, L.; Bao, W. Cerium-Stabilized Cu-SSZ-13 Catalyst for the Catalytic Removal of NO_x by NH_3. *Ind. Eng. Chem. Res.* **2016**, *55*, 1174–1182. [CrossRef]
24. Kim, Y.J.; Lee, J.K.; Min, K.M.; Hong, S.B.; Nam, I.; Cho, B.K. Hydrothermal stability of CuSSZ13 for reducing NO_x by NH_3. *J. Catal.* **2014**, *311*, 447–457. [CrossRef]
25. Xue, J.; Wang, X.; Qi, G.; Wang, J.; Shen, M.; Li, W. Characterization of copper species over Cu/SAPO-34 in selective catalytic reduction of NO_x with ammonia: Relationships between active Cu sites and de-NO_x performance at low temperature. *J. Catal.* **2013**, *297*, 56–64. [CrossRef]
26. Adachi, G.; Imanaka, N. The Binary Rare Earth Oxides. *Chem. Rev.* **1998**, *98*, 1479–1514. [CrossRef]
27. Kwon, D.W.; Nam, K.B.; Hong, S.C. The role of ceria on the activity and SO_2 resistance of catalysts for the selective catalytic reduction of NO_x by NH_3. *Appl. Catal. B Environ.* **2015**, *166–167*, 37–44. [CrossRef]
28. Cao, Y.; Lan, L.; Feng, X.; Yang, Z.; Zou, S. Cerium promotion on the hydrocarbon resistance of a Cu-SAPO-34 NH_3-SCR monolith catalyst. *Catal. Sci. Technol.* **2015**, *5*, 4511–4521. [CrossRef]
29. Han, S.; Cheng, J.; Zheng, C.; Ye, Q.; Cheng, S.; Kang, T.; Dai, H. Effect of Si/Al ratio on catalytic performance of hydrothermally aged Cu-SSZ-13 for the NH_3-SCR of NO in simulated diesel exhaust. *Appl. Surf. Sci.* **2017**, *419*, 382–392. [CrossRef]
30. Zhang, T.; Qiu, F.; Li, J. Design and synthesis of core-shell structured meso-Cu-SSZ-13@mesoporous aluminosilicate catalyst for SCR of NO_x with NH_3: Enhancement of activity, hydrothermal stability and propene poisoning resistance. *Appl. Catal. B Environ.* **2016**, *195*, 48–58. [CrossRef]
31. Gao, F.; Washton, N.M.; Wang, Y.; Kollár, M.; Szanyi, J.; Peden, C.H.F. Effects of Si/Al ratio on Cu/SSZ-13 NH_3-SCR catalysts: Implications for the active Cu species and the roles of Brønsted acidity. *Catal. Today* **2014**, *231*, 64–74. [CrossRef]
32. Wang, D.; Zhang, L.; Li, J.; Kamasamudram, K.; Epling, W.S. NH_3-SCR over Cu/SAPO-34–Zeolite acidity and Cu structure changes as a function of Cu loading. *Catal. Today* **2014**, *231*, 64–74. [CrossRef]

33. Szanyi, J.; Kwak, J.H.; Zhu, H.; Peden, C.H. Characterization of Cu-SSZ-13 NH_3 SCR catalysts: an in situ FTIR study. *Phys. Chem. Chem. Phys.* **2013**, *15*, 2368–2380. [CrossRef] [PubMed]
34. Wang, J.; Yu, T.; Wang, X.; Qi, G.; Xue, J.; Shen, M.; Li, W. The influence of silicon on the catalytic properties of Cu/SAPO-34 for NO_x reduction by ammonia-SCR. *Appl. Catal. B Environ.* **2012**, *127*, 137–147. [CrossRef]
35. Onida, B.; Gabelica, Z.; Lourenco, J.; Garrone, E. Spectroscopic characterization of hydroxyl groups in SAPO-40. 1. Study of the template-free samples and their interaction with ammonia. *J. Phys. Chem. C* **1996**, *100*, 11072–11079. [CrossRef]
36. Zhu, H.; Kwak, J.H.; Peden, C.H.F.; Szanyi, J. In situ DRIFTS-MS studies on the oxidation of adsorbed NH_3 by NO_x over a Cu-SSZ-13 zeolite. *Catal. Today* **2013**, *205*, 16–23. [CrossRef]
37. Wang, L.; Li, W.; Qi, G.; Wen, D. Location and nature of Cu species in Cu/SAPO-34 for selective catalytic reduction of NO with NH_3. *J. Catal.* **2012**, *289*, 21–29. [CrossRef]
38. Sommer, L.; Mores, D.; Svelle, S.; Stöcker, M.; Weckhuysen, B.M.; Olsbye, U. Mesopore formation in zeolite H-SSZ-13 by desilication with NaOH. *Microporous Mesoporous Mater.* **2010**, *132*, 384–394. [CrossRef]
39. Li, Y.; Deng, J.; Song, W.; Liu, J.; Zhao, Z.; Gao, M.; Wei, Y.; Zhao, L. Nature of Cu species in Cu-SAPO-18 catalyst for NH_3-SCR:combination of experiments and DFT calculations. *J. Phys. Chem. C* **2016**, *120*, 14669–14680. [CrossRef]
40. Hun, K.; Zhu, H.; Lee, J.; Peden, C.; Szanyi, J. Two different cationic positions in Cu-SSZ-13? *Chem. Commun.* **2012**, *48*, 4758–4760.